Mechanical and Thermoelectric Properties of Eutectic Composite (Bi, Sb)₂Te₃/Te Thermoelectric Material

Femi Emmanuel Olu[1] · Soon-Jik Hong[2] · Kamanio Chattopadhyay[3]

Abstract Microstructural length scale of an eutectic alloy can be tuned with different cooling rates obtainable via different processing routes, such as melt spinning, suction casting and gas atomization. In this report, the thermoelectric and mechanical properties of selenium-free n-type BiSbTe compound were investigated. One kilogram of powder with a nominal composition of $Bi_{22.5}Sb_{7.5}Te_{70}$ was fabricated using gas atomization. The powders were consolidated into a pellet using spark plasma sintering to minimize rapid grain growth, and the morphologies were examined using scanning electron microscope and X-ray diffraction techniques. The microstructure of the pellet reveals a random eutectic plate-like morphology between the primary phase and Te. The presence of Te results in excess charge carrier injection leading to a high electrical conductivity, while the reduction in length scale in the atomized samples has contributed to the decrease in the mobility of the charge carriers leading to a reasonably good Seebeck coefficient. This microstructure feature is also responsible for the high room temperature micro-Vickers hardness and a 40% reduction in the thermal conductivity. The observed thermoelectric and mechanical properties in this gas atomization + spark plasma sintering have been compared to an earlier reported processing route of flame melting. The relationship between the observed properties and microstructure features is discussed in detail.

1 Introduction

Bismuth telluride-based alloys continue to dominate as the state-of-the-art material for use in solid-state power generation and waste heat recovery at room temperature [1–3]. The efficiency of a thermoelectric material is determined by a quantity called the thermoelectric figure of merit which relates three inter-dependent material's properties such as the Seebeck coefficient (α), electrical conductivity (σ), and the total thermal conductivity (both electronic and phonon contribution) according to the expression $ZT = \alpha^2\sigma/\kappa$. To achieve a good ZT by looking at the expression, the material of choice must possess a high power factor ($\alpha^2\sigma$) and a low thermal conductivity. However, the non-mutually exclusive nature of these material properties makes this a very difficult task. Therefore, research interest in the recent past has been focused on reducing the lattice contribution to the total thermal conductivity [4, 5]. Research approach such as nanostructuring, nanoinclusions, nanocomposites, and microstructure designs that are capable of scattering phonons over a broad range of frequencies have been very successful in reducing lattice contribution to the total thermal conductivity and in some cases have even resulted in the improvement in the power factor leading to an overall enhancement of the ZT [6–10]. Likewise, new proposition of the importance of improving the power factor and research geared toward the

✉ Femi Emmanuel Olu
foluemm@gmail.com

1 Faculty of Materials Science and Engineering, Jimma Institute of Technology, Jimma University, P.O. Box 378, Jimma, Ethiopia

2 Division of Advanced Materials Engineering, Kongju National University, 275, Budae-dong, Cheonan City, Chungcheongnam-do 330-717, Republic of Korea

3 Department of Materials Engineering, Indian Institute of Science, Bangalore, Karnataka 560012, India

improvement in power factor for the overall enhancement of ZT have gained attention in the recent past [11–13]. However, as suggest by Puneet et al. [14], there are other limiting factors that prevent the large-scale transitions of thermoelectric materials (device) from niche laboratory applications to an industrial-scale application such as power generation. Likewise, in a review article, LeBlanc argues that system-level performance of thermoelectric modules relies on more factors than the traditional thermoelectric material performance metrics alone [15]. One of these factors is the mechanical stability and sturdiness of these thermoelectric materials used for the fabrication of thermoelectric devices and modules. This is a direct consequence of repeated heating/cooling cycle and machine handling during device fabrication. Interestingly, Case et al. [16] and Simard et al. [17] argued that the inherent nature of some thermoelectric material is that, they are typically brittle semiconductor making them unlikely to survive, especially under repeated thermal cycling and machine handling during fabrication of thermoelectric device. The control of microstructure in bulk thermoelectric material to combat this drawback is becoming of great interest for the enhancement of thermal and mechanical properties of thermoelectric materials. It has been predicted that different sizes of particles, their microstructure and nature of interfaces obtained in a microstructure during solidification are all expected to influence the thermoelectric transport properties [18, 19]. The microstructures obtained during solidification can be fine-tuned to achieve finer particle size, higher density of interfaces and reduced lamellar spacing in case of eutectic composition via enhanced cooling rate [19]. Eutectic composite in the PbTe-Ge system shows a combination of promising thermoelectric properties and reduced brittleness [20]. Sootsman et al. reported that in PbTe-Si eutectic alloy, secondary phases embedded in microstructure significantly increase their mechanical strength without influencing the thermoelectric performance if composition is selected judiciously [21]. In another work, low lattice thermal conductivity is recorded in a PbTe–Sb_2Te_3 eutectic composite as the spacing between the alternating layers decreases. The decrease in lattice thermal conductivity can be attributed to phonon scattering at the interface of these layers [19].Other eutectic morphologies in lead-free system that are mechanically robust and with good thermoelectric performance have been reported in the literature over the past few years [22, 23]. However, we have first reported eutectic composite in the Bi–Sb–Te system of the type (Bi, $Sb)_2Te_3$/Te synthesized through a simple solidification-processing route of flame melting with good prospect for thermoelectric application [6, 7]. In this work, we have explored the possibility of changing the microstructure morphology of the (Bi, $Sb)_2Te_3$/Te eutectic composite via a

different route and compared the thermoelectric and mechanical properties to an earlier report of the same composition (Ref. [6]).

2 Experimental Procedure

For the gas-atomized sample, elemental pieces of Bi (Alfa Aesar 99.99999%), Sb (Alfa Aesar 99.9999%), and Te (ITΛSCO 99.99999%) corresponding to an hypoeutectic composition $Bi_{22.5}Sb_{7.5}Te_{70}$ on the pseudo-binary phase diagram of Bi-Sb–Te system [24] were measured and melted in an induction furnace to a molten state. Using a sealed nitrogen gas atomizer, the molten mixture was rapidly solidified to form powder. The design and steps involved in the gas atomization process have been fully covered elsewhere [25]. The resultant powders were collected and examined for phase formation by an X-ray diffraction technique on a Miniflex-600 (Rigaku, Japan) with a CuKα source. The morphology of the initial powder was determined on a MIRA3 TESCAN scanning electron microscope (SEM) made in Czech Republic and equipped with a Bruker-made EDS detector. The powders were then spark plasma sintered into bulk using a graphite mold of 30 mm diameter at 400 °C for 10 min. To determine secondary phase formation and the morphology of the sample after SPS, X-ray diffraction analysis and backscattered secondary electron imaging on an SEM were carried out. The compositions of the different phases were examined with the onboard EDS detector at ten different spots and the average was taken as the composition of such phase. The Seebeck coefficient and electrical conductivity of the samples were determined simultaneously using a TEP-1000 thermoelectric properties measurement system in a direction perpendicular to the pressing direction from 300 to 400 K with a sample dimension of 4 × 4 × 10 mm. In order to check reproducibility, the Seebeck measurements were repeated on a commercially available ZEM-3 M10 Ulvac-Riko Seebeck and electrical conductivity measurement unit. The ZEM-3 M10 Ulvac-Riko setup measures the temperature-dependent Seebeck coefficient and electrical resistivity simultaneously using the four-probe method. These measurements were conducted from room temperature to 500 K.

The carrier concentrations were estimated by the Hall effect technique. The total thermal conductivity of the sample was determined in the same direction as the pressing temperature using the laser flash techniques on LFA 447 thermal analyzer by NETZSCH. The experimental procurement followed for the flame-melted samples (Ref. [6]) has been reported elsewhere [6]. The densities of the samples measured by the Archimedes principles were

7440 kg/m^3 for the gas-atomized + SPS sample and 7298 kg/m^3 for the flame-melted sample.

For comparative studies of the mechanical behavior of the gas-atomized + SPS and flame-melted samples, micro-Vickers hardness testing was performed randomly on a polished surface at forty different locations using a 25 gf load for 10 s on an MMT-X3 (Japan) hardness tester. It is important to note that the thermoelectric properties of the flame-melted samples have been reported in our earlier work but not the mechanical properties [6]. Therefore, in this report we compared the thermoelectric and mechanical properties of the gas-atomized + SPS route to that of the flame melting route.

3 Result and Discussion

3.1 Phase and Microstructure Analysis

The X-ray diffraction (XRD) pattern obtained for the gas-atomized powder (Ga powder) is compared to the standard Te and Bi_2Te_3 and presented in Fig. 1. Diffraction peaks with shoulders are clearly visible in the diffraction patterns. The peaks correspond to the Bi_2Te_3 rhombohedral phase with ICSD #01-085-0439, while the shoulders represent the Te phase with ICSD#01-078-2312, as shown in the inset of Fig. 1. However, the XRD pattern obtained after SPS presented in Fig. 2 does not show the presence of the Te phase and a complete disappearance of the shoulder-like peaks is obtained from the powders before the SPS. It should also be noted that the peaks corresponding to $BiSbTe_3$ are also not present compared to our earlier report of the same composition in the flame-melting process [6, 7]. This can probably be attributed to the oversaturation of Sb in the Bi_2Te_3 matrix due to high cooling rate of the gas atomization process. Likewise, Bi_2Te_3 and $BiSbTe_3$ belong to the same crystal structure and space group with close values of lattice parameters and this can result in additional difficulties in phase identification in the powder XRD pattern.

Figure 3a represents the powder morphology after gas atomization. The powder shows a spherical morphology with a bimodal particle distribution with an average size of 15–20 μm for the smaller particle and 100–110 μm for the bigger particle, as shown in Fig. 3c. The microstructure of the bulk sample after spark plasma sintering is shown in Fig. 3b. The backscattered secondary electron images show a eutectic plate-like morphology with bright and dark phases. The bright phase constitutes the matrix phase with a composition of $Bi_{26}Sb_{11}Te_{62}$ identified as $(Bi, Sb)_2Te_3$, while the dark phase reveals a composition that is mostly Te, as shown in Table 1. In comparison with earlier report of references [5] and [6] that show a microstructure consisting of a matrix phase and colonies of eutectics, the microstructure obtained in the present case is composed of only plate-like eutectic of $(Bi, Sb)_2Te_3$ and the Te phases. The areas marked in Fig. 3b are probably the bigger particles, and magnified image of this region is shown in Fig. 3d.

3.1.1 Mechanical Properties

Figure 4 presents the micro-Vickers hardness and fracture surfaces of the gas-atomized + SPS and flame-melted samples measured at room temperature. The mechanical properties of the flame-melted sample are reported for the first time in this report. The gas-atomized + SPS sample shows a high room temperature hardness of 75.3 Hv, while

Fig. 1 X-ray diffraction pattern of the as-atomized powder: The peaks correspond to the Bi_2Te_3 rhombohedral phase with ICSD #01-085-0439, and shoulder at the most intense peak represents the Te phase with ICSD #01-078-2312 as shown in the inset
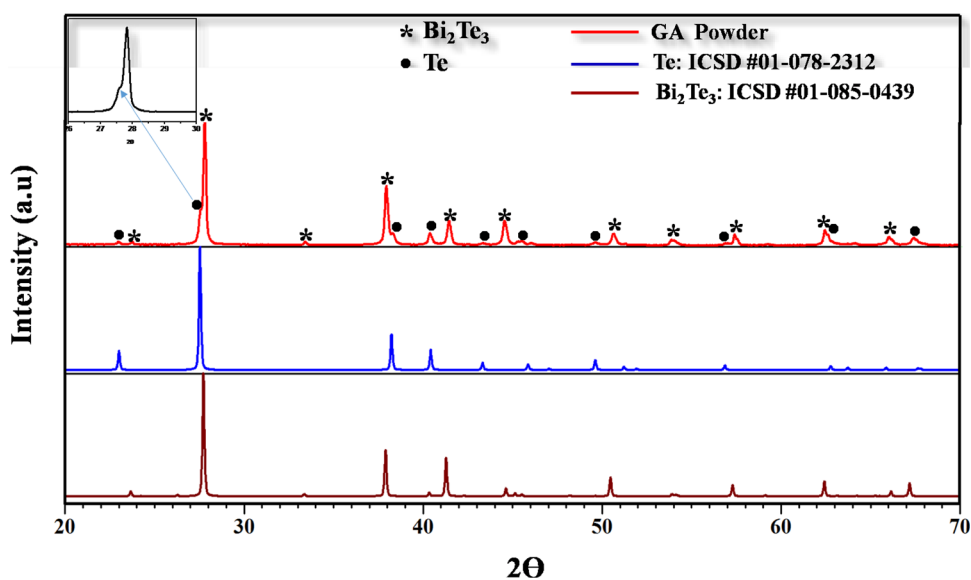
Fig. 2 X-ray diffraction pattern of the gas-atomized powder + SPS: The XRD pattern obtained shows a complete disappearance of the shoulder-like peaks seen in Fig. 1. The peaks correspond to the Bi_2Te_3 rhombohedral phase with ICSD #01-085-0439 with the absence of the Te phase
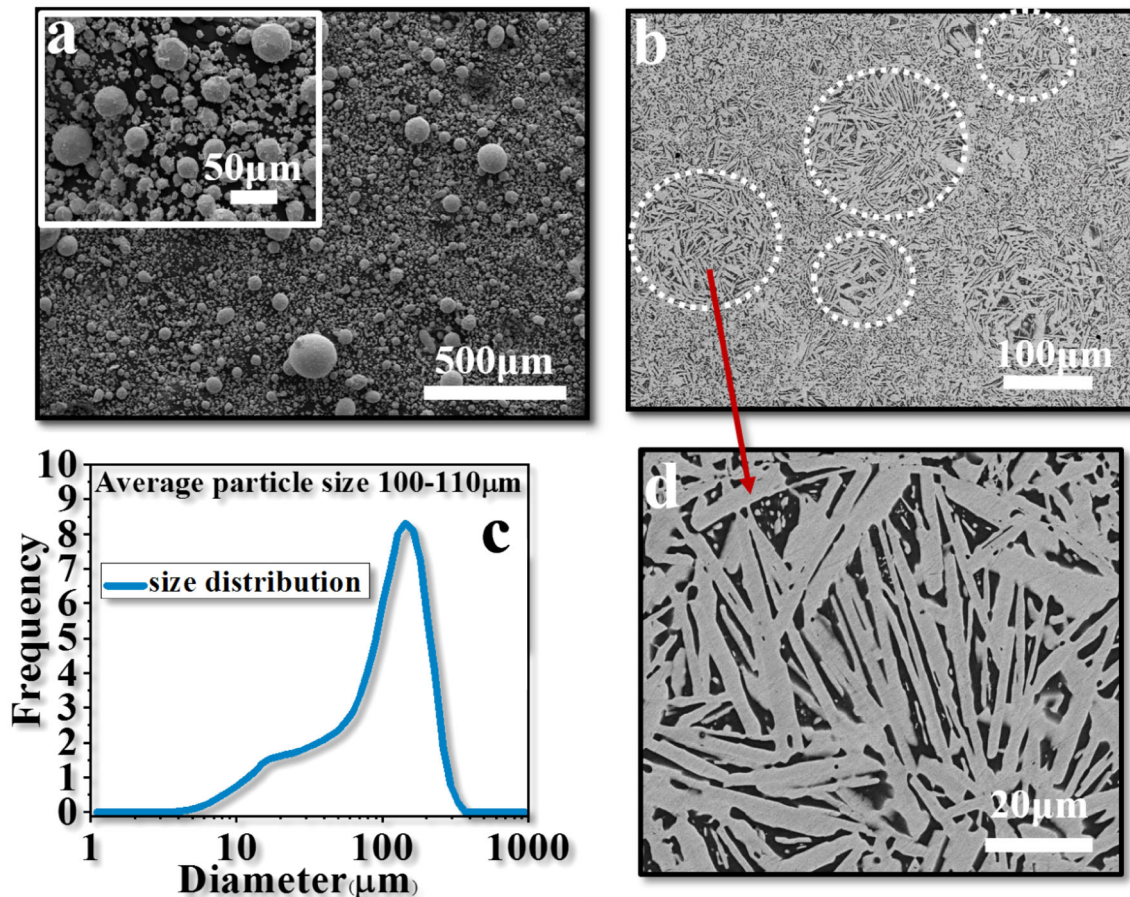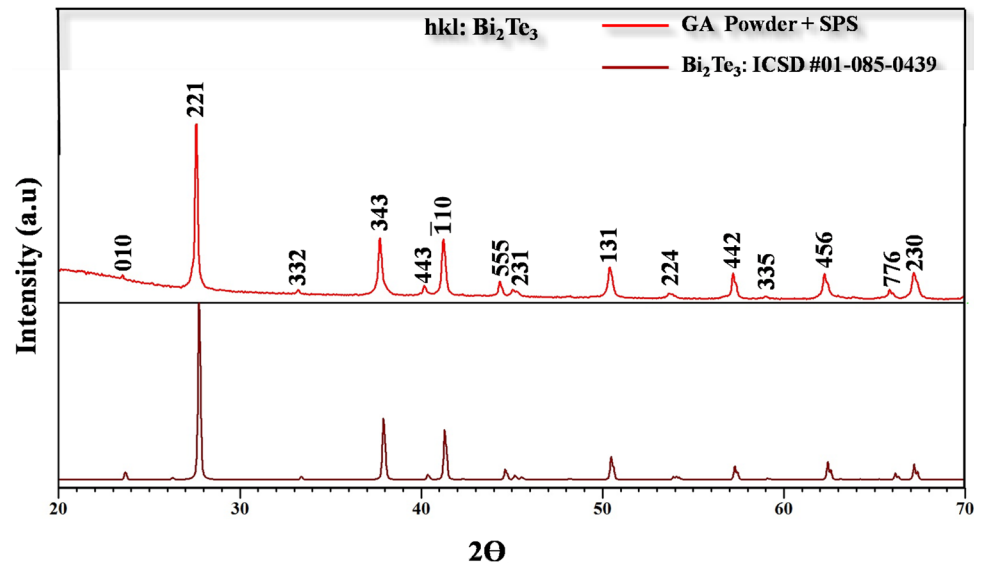

Fig. 3 Secondary electron and backscattered secondary electron image: **a** powder morphology after gas atomization showing spherical particle of different sizes as shown in (**c**). **b** BSE image of the gas atomization + SPS showing random eutectic plate-like morphology. **c** powder size analyses after gas atomization showing bimodal particle size distribution. **d** High magnification image of b showing the formation of eutectic between the primary phase and Te

Table 1 Summary of composition measure via the energy-dispersive techniques at the different phases on the microstructure and the average taken as the composition of such phase

Processing technique	Overall composition		Composition of the matrix phase		Composition of the secondary phase	
Gas atomization + SPS	Bi	20.8 ± 2.5	Bi	26.2 ± 1.1	Bi	2.9 ± 1.9
	Sb	8.8 ± 0.3	Sb	11.2 ± 0.6	Sb	3.7 ± 0.5
	Te	70.4 ± 2.8	Te	62.3 ± 0.7	Te	95.4 ± 3.8
	Total	100	Total	99.7	Total	102

Fig. 4 Mechanical properties of the gas-atomized + SPS and the flame-melted sample: **a** micro-Vickers hardness for the gas-atomized + SPS sample showing limited crack propagation's **b** micro-Vickers hardness for the flame-melted sample showing easy crack propagation and longer crack length. **c–d** Fracture surfaces of both sample showing transgranular mode of fracture
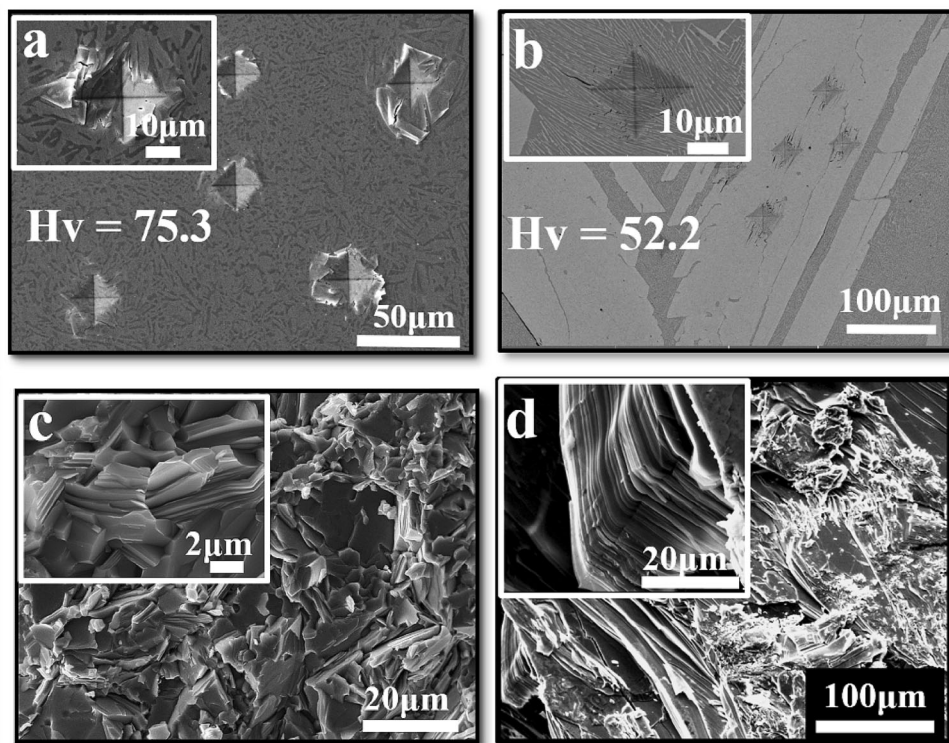
the flame-melted sample has a value of 52.3 Hv. These results can be associated with the microstructural features observed in both the processing routes, as shown in Fig. 4a, b. The random eutectic mixture of the primary and secondary phases and the smaller grain size of the phases in the gas-atomized + SPS sample as shown in Fig. 3 create an abundance of grain boundaries and interfaces. These are responsible for the high room temperature hardness because crack propagation is more effectively inhibited by these random plate-like eutectic mixtures in the gas-atomized + SPS sample unlike the eutectic in the flame-melted sample, which are not randomly distributed and rather forming colonies leading to easy crack propagation both within the eutectic colonies and also in the primary phase. Transgranular mode of fracture is observed on the fracture surfaces of both the samples, as shown in Fig. 4c, d.

3.2 Transport Properties Analysis

Figure 5a represents the electrical conductivity (σ) of the bulk sample. In comparison with the result obtained in reference [6] (Red plot), the electrical conductivity shows a metal-like behavior with a minimum of 120 S/m at 300 K compared to 90 S/m at 300 K obtained in reference [6] (Red plot). Across the measured temperature range, the gas-atomized sample shows the highest electrical conductivity compared to the values reported in reference [6] (Red plot) for similar starting compositions. The high electrical conductivity obtained for the gas-atomized samples can be attributed to the high carrier concentration, as shown in Table 2 due to charge carrier injection owing to the presence of Te phase [6]. However, the high density of interfaces shown in Fig. 3b has resulted in the decrease in the carrier mobility in the gas-atomized + SPS sample

Fig. 5 Temperature-dependent transport properties: **a** electrical conductivity. The gas-atomized + SPS shows the highest electrical conductivity despite the abundance of grain boundary and interfaces. **b** Seebeck coefficient. The negative sign of the Seebeck coefficient shows that electron is the dominant carrier. **c** The power factor. The power factor is estimated from the Seebeck coefficient and electrical conductivity. **d** Thermal conductivity. There is a 40% reduction in the thermal conductivity of the gas-atomized + SPS sample due to the abundance of grain boundaries and interfaces (color figure online)
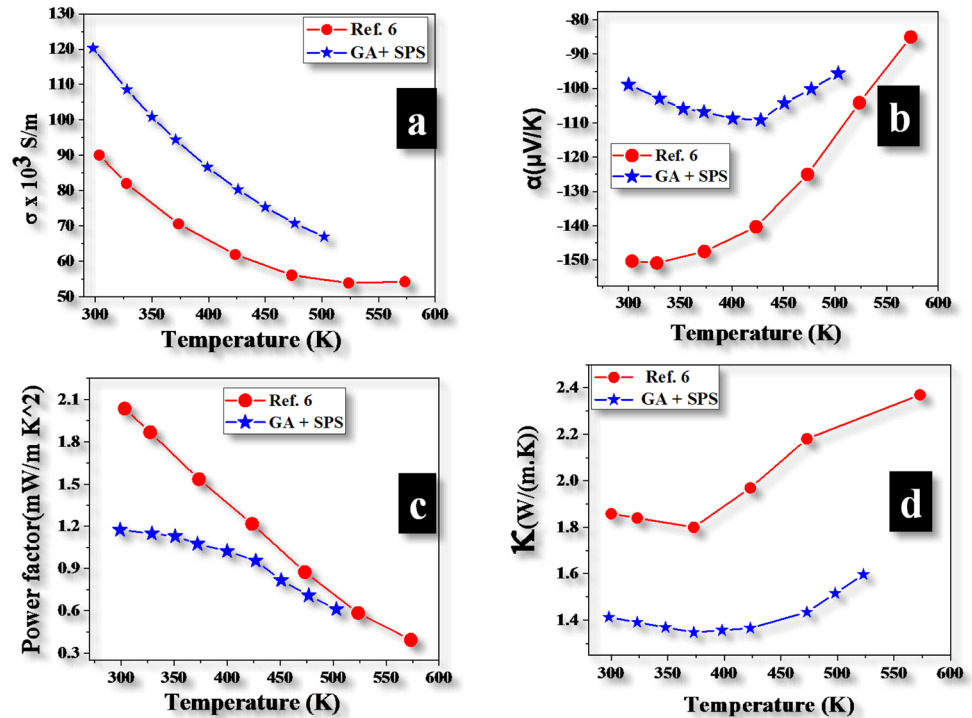

Table 2 Estimation of carrier concentration using Hall measurement; the increase in the carrier concentration in the gas-atomized + SPS sample is due to the interfacial charge defect resulting in excess injection of charge carriers
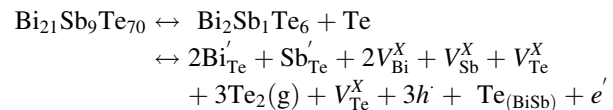
Technique	n (cm^3)	μ (cm^3/V s)
Gas atomization + SPS	7.37×10^{19}	89
Flame melting (7)	3.5×10^{19}	160.8

compared to the flame-melted sample, as shown in Table 2. This implies that the length scale of the interfaces between Te and (Bi, Sb)$_2$Te$_3$ in the gas-atomized + SPS sample is probably of the same order of magnitude as the mean-free-path of the charge carriers leading to a reduction in the mobility of the charge carriers [19].

The Seebeck coefficient (α) for the bulk sample is shown in Fig. 5b. At a first glance, the magnitude of the Seebeck coefficient shows an increasing trend with temperature to a maximum (109 V/K) at 428 K before decreasing with further increase in temperature. The negative sign of the Seebeck coefficient indicates that electrons are primarily responsible for carrier transport. In comparison with the results obtained in reference [6] (Red plot), the maximum magnitude of the Seebeck coefficient is (155 V/K) at 325 K.

Conventionally, in BiSbTe thermoelectric material, the presence of antisite defects and changes in stoichiometry determine the dominant carrier type and conductivity in these samples. In this case, the equilibrium defect

equations keeping in mind the dominant phases of the bulk composition after SPS shown in Fig. 3b and Table 1 can be approximately written as

$$Bi_{21}Sb_9Te_{70} \leftrightarrow Bi_2Sb_1Te_6 + Te$$
$$\leftrightarrow 2Bi'_{Te} + Sb'_{Te} + 2V^X_{Bi} + V^X_{Sb} + V^X_{Te}$$
$$+ 3Te_2(g) + V^X_{Te} + 3h^{\cdot} + Te_{(BiSb)} + e'$$

where e' denotes an electron, $h^{\bullet}$ holes, V^x vacancies and superscript denote the formal charge of the particles. The presence of the substitutional point defects $Te^{\bullet}_{(BiSb)}$ and Te vacancies lead to the decrease in the Bi'_{Te} and Sb'_{Te} antisite defect therefore creating an *n*-type conductivity. The substitutional point defect and Te vacancies suppress the hole formation by injecting excess electron into the lattice as seen in the equation. Likewise, the injection of excess electron by the positively charged substitutional point defect and Te vacancies lead to low electrical resistivity despite large presence of interfaces observed in the microstructure [7, 14, 26]. This is confirmed by the high carrier concentration shown in Table 2 by Hall measurement. The high carrier concentration in the sample made by gas atomization + SPS results in the high electrical conductivity shown in Fig. 5a compared to that reported in reference [6] (Red plot). From Table 2, although the sample of reference [6] shows a higher carrier mobility compared to that of the gas-atomized + SPS sample, the electrical conductivity has a direct dependence on both the carrier concentration and carrier mobility. Therefore, the contribution of the carrier concentration in

Table 3 Estimation of the thermal bandgap using the temperature-dependent Seebeck coefficient and resistivity measurement

Technique	$|S_{max}|$ (μV/K)	T_{max} (K)	Goldsmid–Sharp thermal bandgap (eV)	Thermal bandgap estimated from the resistivity measurement (eV)
GA + SPS	109	428	0.093	0.0752
Flame melting (7)	150	327	0.098	0.0606

The Goldsmid–Sharp thermal bandgap was estimated using the formula $E_g = 2e|S_{max}|T_{max}$ from the temperature-dependent Seebeck coefficient and the slope of $Log_{10}\rho$ Vs $10^3/T$ from the temperature-dependent resistivity measurement. The Goldsmid–Sharp thermal bandgap of the flame-melted sample has been earlier reported elsewhere (7)
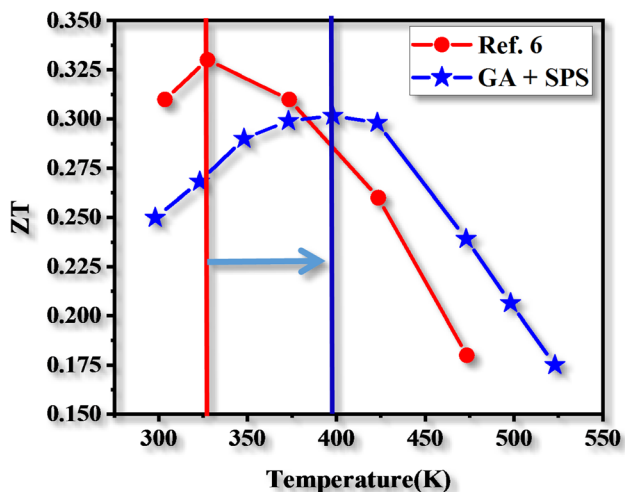

Fig. 6 Thermoelectric figure of merit (ZT) of the GA + SPS and the flame-melted samples [6, 7]. The GA + SPS sample shows a maximum ZT of 0.3 at 398 K, while the flame-melted sample as reported earlier reveals a ZT of 0.33 at 327 K. The operating temperature of the GA + SPS has shifted to higher temperature even with a negligible decrease in the ZT value. This can be attributed to the delay in the onset of the bipolar contribution

the gas-atomized + SPS samples far outweigh the contribution of the carrier mobility to the observed electrical conductivity. Below 428 K, the Seebeck coefficient for the gas-atomized + SPS samples increases with increasing temperature according to the Mott and Jones [27] formula given as

$$\alpha = \frac{\pi^2 K_B^2 T}{3e} \frac{d}{dE} [\ln \sigma(E)]_{E=E_f} \tag{1}$$

where k_B is the Boltzmann constant, T is the absolute temperature, e is the electronic charge, E is the energy level of the electron, and E_f is the Fermi energy [28]. Above 428 K, the decrease in the Seebeck coefficient with increasing temperature can be attributed to thermally excited carriers corresponding to the temperature dependency of electrical conductivity [29]. Likewise, these thermally excited carriers lead to bipolar contribution at high temperature resulting in excess charge carriers and a

reduction in the Seebeck coefficient [7, 30]. The maximum values of the Seebeck coefficient have been used to estimate the thermal bandgap of each of the samples by following the method reported by Goldsmid–Sharp [31] as shown in Table 2. It should be noted that Gibbs et al. cautioned that the use of the method can lead to small deviations from the actual thermal bandgap for $|S_{max}|$- < 150 K. Likewise, the temperature-dependent resistivity values have been used to estimate the thermal bandgap for the samples as well and the values show a little deviation from the values obtained from the Goldsmid–Sharp method. The limitation in these methods leads to the slight deviations in the two methods as enumerated by Gibbs et al. [32] in their report on half-Heusler alloy. The Ga + SPS samples show an upshift in the onset of bipolar contribution to a higher temperature compared to the flame-melted sample even though the thermal bandgap is approximately closer in value to the thermal bandgap of the flame-melted sample. This upshift in the onset of bipolar contribution can be attributed to the charge carrier filtering at the interfaces of the Ga + SPS samples, thereby delaying the contribution of the minority carrier to the Seebeck coefficient to a higher temperature [33].

Figure 4c represents the power factor ($\alpha^2\sigma$) obtained from the temperature-dependent electrical conductivity and the Seebeck coefficient, respectively. Compared to the reported values of Ref. [6], the gas-atomized + SPS sample shows a lower power factor. This can be attributed to the superior values of Seebeck coefficient reported in Ref. [6] even though the electrical conductivity is lesser than the gas-atomized + SPS (Table 3).

The temperature-dependent thermal conductivity is shown in Fig. 5d. The gas-atomized + SPS sample shows a 40% reduction in thermal conductivity compared to the flame-melted sample reported in Ref. [6] at room temperature. At $T < 375$, the thermal conductivity decreases with increasing temperature for both the gas-atomized + SPS sample and the flame-melted sample reported in Ref. [6]. As explained in our earlier reports, the thermal conductivity in the temperature regime shows an inverse

relationship with temperature ($K \propto 1/T$) indicating grain boundary/interface and phonon–phonon scattering [7, 14]. The microstructure of the gas-atomized + SPS samples shown in Fig. 3b reveals abundant of grain boundaries and interfaces compared to the reported microstructure of Ref. [6], which serve as phonon scarring centers resulting in a reduction in thermal conductivity. In other reports, room temperature deformation and hot plastic deformation have been proposed as a viable mechanism to achieve ultra-low thermal conductivity in Bi_2Te_3-type materials [34, 35].

The upward increase in the thermal conductivity beyond 374 K is a common occurrence in Bi–Sb–Te-type compound, which in the literature has been attributed to the bipolar contribution of both holes and electrons to the heat flow.

This bipolar contribution to the thermal conductivity is expressed as

$$K_B = \frac{\sigma_e \sigma_h (\alpha_e - \alpha_h)^2}{\sigma_e + \sigma_h} T \tag{2}$$

where σ_e, σ_h, α_e and α_h are contributions of electron and hole carriers to the Seebeck coefficient and electrical conductivity, respectively [7, 36].

The power factor of Fig. 5c and the total thermal conductivity of Fig. 5d have been used to estimate the thermoelectric figure of merit (ZT) according to the formula $ZT = \alpha^2 \sigma / \kappa$, where $\alpha^2 \sigma$ is the power factor and κ is the total thermal conductivity and shown in Fig. 6. The ZT of the GA + SPS samples shows a maximum ZT 0.3 at 398 K compared to the earlier reported value of 0.33 at 327 K for the flame-melted sample [6, 7]. Close observation of Fig. 6 shows that the maximum ZT of the GA + SPS sample occurs at a higher operating temperature than the flame-melted sample even with a slightly lower value of ZT. This can be attributed to the delay in the onset of the bipolar contribution in the GA + SPS sample as a result of the abundance of interfaces responsible for charge carrier scarring and energy filtering. The GA + SPS samples show an upshift of 71 °C in operating temperature and a fairly good ZT value compared to the flame-melted sample with an operating temperature at room temperature.

4 Conclusion

In the present study, the thermoelectric and mechanical properties of gas-atomized n-type BiSbTe have been investigated and compared to our earlier report of the same composition but with different processing routes. The microstructure of the gas-atomized + SPS sample shows an eutectic with plate-like morphology of BiSbTe phase along with Te. The presences of Te, as reported earlier, result in charge carrier injection leading to superior electrical conductivity but an inferior Seebeck coefficient. However, the abundance of grain boundaries and interfaces in the gas-atomized + SPS sample results in a 40% reduction in thermal conductivity and is responsible for the high room temperature Vickers hardness. An upshift of 71 °C of the operating temperature of the GA + SPS sample is obtained due to the delay in the onset of bipolar contribution in the sample.

References

1. Petsagkourakis I, Tybrandt K, Crispin X, Ohkubo I, Satoh N, and Mori T *Sci Technol Adv Mater* **19** (2018) 836.
2. Haras M and Skotnicki T, *Nano Energy* **54** (2018) 461.
3. Mori T and Priya S, *MRS Bull* **43** (2018) 176.
4. Rowe D M, **Section D**, *CRC Handbook of Thermoelectrics*, CRC, Boca Raton (1995).
5. Goldsmid H J, *Introduction to Thermoelectricity*. Springer, Berlin (2010).
6. Femi O E, Ravishankar N, and Chattopadhyay K, *J Mater Sci* **51** (2016) 7254.
7. Femi O E, Akkiraju K, Murthy B S, Ravishankar N, and Chattopadhyay K, *J Alloys Compd.* **682** (2016) 791.
8. Vineis C J, Shakouri A, Majumdar A, and Kanatzidis M G, *Adv Mater* **22** (2010) 3970.
9. Faleev S V, and Léonard F, Phys Rev B **77** (2008) 214304.
10. Wu H -J, Foo W -J, Chen S -W, and Jeffrey Snyder G, *Appl Phys Lett* **101** (2012) 023107.
11. Mori T, *Small* **13** (2017) 1702013.
12. Liu W, Kim H S, Jie Q, and Ren Z, *Scr Mater* **111** (2016) 3.
13. Vaney J B, AminorroayaYamini S, Takaki H, Kobayashi K, Kobayashi N, and Mori T, *Mater Today Phys* **9** (2019) 100090.
14. Puneet P, Podila R, Karakaya M, Zhu S, He J, Tritt T M, Dresselhaus M S, and Rao A M, *Sci Rep* **3** (2013) 3212.
15. LeBlanc S, *SM&T.* **1–2** (2014) 26.
16. Case E D, *J Electron Mater* **41** (2012) 1811.
17. Simard J M, Vasilevskiy D, and Turenne S, in Proceedings of 22nd IEEE International Conference on Thermoelectric (IEEE, 2003), pp 13–18.
18. Ikeda T, Ravi V A, and Snyder G J, *Metall Mater Trans A* **41** (2010) 641.
19. Medlin D L, and Snyder G J, *Curr Opin Colloid Interface Sci* **14** (2009) 226.
20. Sootsman J R, He J, Dravid V P, Li C -P, Uher C, and Kanatzidis M G, *J Appl Phys* **105** (2009) 083718.
21. Sootsman J R, He J, Dravid V P, Ballikaya S, Vermeulen D, Uher C, and Kanatzidis M G, *Chem Mater* **22** (2010) 869.
22. Cao Y Q, Zhao X B, Zhu T J, Zhang X B, and Tu J P, *Appl Phys Lett* **92** (2008) 143106.
23. Mukherjee S, Femi O E, Chetty R, Chattopadhyay K, Suwas S, and Mallik R C, *Appl Surf Sci* **1** (2017).
24. Abrikosov NK, *Bi–Sb–Te phase diagram, ASM alloy phase diagram database*, ASM International, Materials Park (1965)

25. Lee C -H, Fatih Kilicaslan M, Madavali B, and Hong S -J, Res. Chem. Intermediate **40**, 2543 (2014).
26. Teweldebrhan D, Goyal V, and Balandin A A, *Nano Lett* **14** (2010).
27. Rohrman F A, *J Chem Educ* **14** (1937) 99.
28. Mott N F, and Jones H, *The Theory of the Properties of Metals and Alloys*, Clarendon Press, Oxford (2016).
29. Ito M, Ohishi Y, Muta H, Kurosaki K, and Yamanaka S, *MRS Proc* **1314** (2011) 405.
30. Zhang L, Xiao P, Shi L, Henkelman G, Goodenough J B, and Zhou J, *J Appl Phys* **117** (2015) 155103.
31. Goldsmid H J, Sharp J W, *J Electron Mater* **28** (1999) 869.

32. Gibbs Z M, Kim H -S, Wang H, and Snyder G J, *Appl Phys Lett* **106** (2015) 022112.
33. Liu M, and Qin X Y, *Appl Phys Lett* **101** (2012) 132103.
34. Fan X A, Yang J Y, Zhu W, Bao S Q, Duan X K, Xiao C J, and Li K, *J Phys D Appl Phys* **40** (2007) 5727.
35. Grasso S, Tsujii N, Jiang Q, Khaliq J, Maruyama S, Miranda M, Simpson K, Mori T, and Reece M J, *J Mater Chem* **1** (2013) 2362.
36. Goldsmid H, and Sharp J, *Energies* **8** (2015) 6451.